

# Mixing of polarization states in zincblende nonlinear optical crystals

PAULINA S. KUO<sup>1,\*</sup> AND M. M. FEJER<sup>2</sup>

<sup>1</sup>Information Technology Laboratory, National Institute of Standards and Technology, 100 Bureau Drive, Gaithersburg, Maryland 20899, USA

<sup>2</sup>E. L. Ginzton Laboratory, Stanford University, 348 Via Pueblo Mall, Stanford, California 94305, USA

\*[paulina.kuo@nist.gov](mailto:paulina.kuo@nist.gov)

**Abstract:** We describe second-order nonlinear optical mixing in non-birefringent, zincblende-structure materials that can be quasi-phasematched. Lack of birefringence and quasi-phasematching together allow efficient nonlinear mixing between diverse polarization states. We derive six coupled-wave equations that describe nonlinear optical mixing between the two orthogonal polarizations of the three frequencies in the second-order nonlinear interaction. The interactions of the additional polarization states can lead to apparent reduction in conversion efficiencies in optical parametric oscillators and amplifiers.

© 2018 Optical Society of America under the terms of the [OSA Open Access Publishing Agreement](#)

## 1. Introduction

Zincblende semiconductors such as GaAs, GaP, and ZnSe are attracting increasing attention for nonlinear optical frequency conversion. These materials have large nonlinear susceptibilities and wide transparency ranges extending far into the infrared. Cubic symmetry in zincblende crystals implies isotropic linear optical properties, which means that birefringent phasematching is not possible in bulk media. The difficulty in achieving phasematching in these materials has historically limited their utility. The development of practical techniques to achieve quasi-phasematching (QPM) [1] has enabled more widespread use of zincblende crystals for nonlinear optics. Epitaxial methods of growing crystals with periodically alternating domain orientations have been developed in GaAs [2–4] and GaP [5, 6]. These quasi-phasematched zincblende materials have been used to demonstrate second-harmonic generation (SHG) [7–9], optical parametric oscillation [10–15], difference frequency generation (DFG) [16–20] and optical parametric generation [21].

High symmetry in the nonlinear susceptibility tensor for zincblende crystals combined with the lack of birefringence allow for efficient mixing of a wide range of polarization states. The only non-zero tensor elements in zincblende-structure ( $\bar{4}3m$  point group) materials are  $d_{xyz}$  and its permutations (namely,  $d_{xyz} = d_{14} = d_{25} = d_{36}$  in contracted notation). As a result, one is no longer constrained to choose waves with specific combinations of linear polarization to access the large non-zero coefficient. QPM allows phasematching to be achieved without relying on birefringence and specific polarization states. Using QPM GaAs, polarization-insensitive DFG [16], and optical parametric oscillation using various linearly polarized pump sources [10], as well as circularly polarized and depolarized pump sources [11] were demonstrated.

In this paper, we build on the description of polarization dependence for nonlinear optical mixing in zincblende crystals presented previously [10, 11, 19, 22]. The additional polarization states participating in the nonlinear processes can affect the overall nonlinear conversion efficiency and enhance back-conversion, especially during high gain or depleted pump conditions, such as those occurring in optical parametric oscillators (OPOs) and optical parametric amplifiers (OPAs).

## 2. Coupled-wave equations

### 2.1. General driving equations

Assume a collinear interaction and assign the propagation axis to  $z'$  along the propagation direction  $\hat{\mathbf{k}}$  (which may be different from the crystallographic  $\hat{\mathbf{z}}$  direction). Typically experiments in QPM zincblende semiconductors like orientation-patterned GaAs (OP-GaAs) and orientation-patterned GaP (OP-GaP) have utilized  $\hat{\mathbf{k}}$  along the  $[\bar{1}10]$  crystallographic direction. We note that propagation along the  $[001]$  direction in zincblende materials will produce no nonlinear optical mixing because the non-zero tensor element  $d_{xyz}$  requires electric field components along all three crystal directions,  $\hat{\mathbf{x}}$ ,  $\hat{\mathbf{y}}$  and  $\hat{\mathbf{z}}$ . If  $\hat{\mathbf{k}}$  is parallel to  $\hat{\mathbf{z}}$  for instance, then there will be no electric field component of any frequency along  $\hat{\mathbf{z}}$ .

In second-order nonlinear mixing between pump ( $\omega_3$ ), signal ( $\omega_2$ ) and idler ( $\omega_1$ ) where  $\omega_3 = \omega_1 + \omega_2$ , the electric field at frequency  $\omega_i$  is given by [23]

$$\mathbf{E}_i(z', t) = \text{Re}[\mathbf{E}_i(z')e^{i(k_i z' - \omega_i t)}], \quad (1)$$

where  $i = 1, 2$  or  $3$  and  $\mathbf{E}_i(z')$  is the slowly varying electric field amplitude. Analogous expressions may be written for the nonlinear polarization,  $\mathbf{P}_i^{(2)}(z', t)$ . If each electric field is written in terms of its amplitude and a unit vector in the direction of its polarization,  $\mathbf{E}_i(z') = E_i \hat{\mathbf{e}}_i$ , then  $\mathbf{P}_i^{(2)}(z', t)$  becomes

$$\begin{aligned} \mathbf{P}_1^{(2)}(z', t) &= \text{Re}[\epsilon_0 E_2^* E_3 (\underline{\underline{\mathbf{d}}} : \hat{\mathbf{e}}_2 \hat{\mathbf{e}}_3) e^{i[(-k_2 + k_3)z' - \omega_1 t]}] \\ \mathbf{P}_2^{(2)}(z', t) &= \text{Re}[\epsilon_0 E_1^* E_3 (\underline{\underline{\mathbf{d}}} : \hat{\mathbf{e}}_3 \hat{\mathbf{e}}_1) e^{i[(-k_1 + k_3)z' - \omega_2 t]}] \\ \mathbf{P}_3^{(2)}(z', t) &= \text{Re}[\epsilon_0 E_1 E_2 (\underline{\underline{\mathbf{d}}} : \hat{\mathbf{e}}_1 \hat{\mathbf{e}}_2) e^{i[(k_1 + k_2)z' - \omega_3 t]}]. \end{aligned} \quad (2)$$

where  $(\underline{\underline{\mathbf{d}}} : \hat{\mathbf{e}}_2 \hat{\mathbf{e}}_3)$  represents the vector resulting from projection of the tensor  $\underline{\underline{\mathbf{d}}}$  on the field directions  $\hat{\mathbf{e}}_2$  and  $\hat{\mathbf{e}}_3$ , and similarly for the other two frequencies.

Only the component of the nonlinear polarization transverse to  $\hat{\mathbf{k}}$  drives the propagating fields. Thus, the slowly varying envelope equations are [23]

$$\begin{aligned} \frac{d\mathbf{E}_1(z')}{dz'} &= i\gamma_1 \mathbf{P}_{1,\text{trans}}^{(2)}(z') e^{i\Delta k z'} \\ \frac{d\mathbf{E}_2(z')}{dz'} &= i\gamma_2 \mathbf{P}_{2,\text{trans}}^{(2)}(z') e^{i\Delta k z'} \\ \frac{d\mathbf{E}_3(z')}{dz'} &= i\gamma_3 \mathbf{P}_{3,\text{trans}}^{(2)}(z') e^{-i\Delta k z'}, \end{aligned} \quad (3)$$

where  $\mathbf{P}_{i,\text{trans}}^{(2)}(z') = \mathbf{P}_i^{(2)}(z') - (\hat{\mathbf{k}} \cdot \mathbf{P}_i^{(2)}(z'))\hat{\mathbf{k}}$ ,  $\gamma_i = \omega_i / (2\epsilon_0 c n_i)$ , and  $\Delta k = k_3 - k_1 - k_2$ .

Each of the vector quantities in  $\mathbf{E}_i(z')$  and  $\mathbf{P}_{i,\text{trans}}^{(2)}(z')$  can be projected onto two orthogonal axes transverse to  $\hat{\mathbf{k}}$ . The use of a single  $\Delta k$  in Eq. (3) is appropriate only for isotropic media such as the zincblende semiconductors, or when propagating along an optical axis of a birefringent crystal. What typically happens in birefringent crystals is that only one combination of pump, signal and idler polarizations is phase-matched, which enables neglect of the other three field components and thus reduction of Eq. (3) to three scalar equations. However, by using QPM in non-birefringent crystals, phase-matching no longer constrains the polarization states that can participate in the interactions so that Eqs. (3) represents six scalar equations instead of three. The dynamics described by these equations can be very rich, some aspects of which we explore in this paper.

## 2.2. Amplitude and orientation equations

The six coupled-wave equations in Eq. (3) can be cast in terms of the amplitudes and polarization-orientation angles of the interacting waves. In this discussion, we will limit ourselves to linear polarization states and assume isotropic refractive indices. Let us consider linearly polarized, orthogonal unit vectors ( $\hat{\mathbf{a}}, \hat{\mathbf{b}}$ ) in the plane orthogonal to  $\hat{\mathbf{k}}$ . For the typical geometry in OP-GaAs and OP-GaP,  $\hat{\mathbf{k}}$  is parallel to  $[\bar{1}10]$ , and the transverse basis can be chosen as  $\hat{\mathbf{a}}$  along  $[110]$  and  $\hat{\mathbf{b}}$  along  $[001]$ . We can write  $\mathbf{E}_i(z')$  as

$$\begin{aligned}\mathbf{E}_i &= E_i \hat{\boldsymbol{\theta}}_i, \\ \hat{\boldsymbol{\theta}}_i &= \cos \theta_i \hat{\mathbf{a}} + \sin \theta_i \hat{\mathbf{b}},\end{aligned}\quad (4)$$

where  $E_i$  is the amplitude of the field,  $\theta_i$  is the orientation angle of  $\mathbf{E}_i$  relative to  $\hat{\mathbf{a}}$ . We note that  $\hat{\boldsymbol{\theta}}_i$  differ from  $\hat{\mathbf{e}}_i$  discussed in section 2.1 in that  $\hat{\boldsymbol{\theta}}_i$  are by construction perpendicular to the propagation direction  $\hat{\mathbf{k}}$  whereas  $\hat{\mathbf{e}}_i$  refer to generic electric field polarizations. The derivative of  $\mathbf{E}_i$  with respect to  $z'$  is

$$\begin{aligned}\frac{d\mathbf{E}_i}{dz'} &= \frac{d}{dz'} (E_i \hat{\boldsymbol{\theta}}_i) \\ &= \frac{dE_i}{dz'} \hat{\boldsymbol{\theta}}_i + E_i \frac{d\theta_i}{dz'} \hat{\boldsymbol{\theta}}_{i,\perp},\end{aligned}\quad (5)$$

where  $\hat{\boldsymbol{\theta}}_{i,\perp} = -\sin \theta_i \hat{\mathbf{a}} + \cos \theta_i \hat{\mathbf{b}}$  is a unit vector orthogonal to  $\hat{\boldsymbol{\theta}}_i$ .

Combining Eqs. (3) and (5) and assuming  $\Delta k = 0$ , it follows that

$$\begin{aligned}\frac{dE_1}{dz'} &= i\kappa_1 E_2^* E_3 \hat{\boldsymbol{\theta}}_1 \cdot (\underline{\mathbf{d}}' : \hat{\boldsymbol{\theta}}_2 \hat{\boldsymbol{\theta}}_3) = i\kappa_1 E_2^* E_3 f_1(\theta_1; \theta_2, \theta_3) \\ \frac{dE_2}{dz'} &= i\kappa_2 E_3 E_1^* \hat{\boldsymbol{\theta}}_2 \cdot (\underline{\mathbf{d}}' : \hat{\boldsymbol{\theta}}_3 \hat{\boldsymbol{\theta}}_1) = i\kappa_2 E_3 E_1^* f_2(\theta_2; \theta_3, \theta_1) \\ \frac{dE_3}{dz'} &= i\kappa_3 E_1 E_2 \hat{\boldsymbol{\theta}}_3 \cdot (\underline{\mathbf{d}}' : \hat{\boldsymbol{\theta}}_1 \hat{\boldsymbol{\theta}}_2) = i\kappa_3 E_1 E_2 f_3(\theta_3; \theta_1, \theta_2) \\ E_1 \frac{d\theta_1}{dz'} &= i\kappa_1 E_2^* E_3 \hat{\boldsymbol{\theta}}_{1,\perp} \cdot (\underline{\mathbf{d}}' : \hat{\boldsymbol{\theta}}_2 \hat{\boldsymbol{\theta}}_3) = i\kappa_1 E_2^* E_3 f_{1,\perp}(\theta_1; \theta_2, \theta_3) \\ E_2 \frac{d\theta_2}{dz'} &= i\kappa_2 E_3 E_1^* \hat{\boldsymbol{\theta}}_{2,\perp} \cdot (\underline{\mathbf{d}}' : \hat{\boldsymbol{\theta}}_3 \hat{\boldsymbol{\theta}}_1) = i\kappa_2 E_3 E_1^* f_{2,\perp}(\theta_2; \theta_3, \theta_1) \\ E_3 \frac{d\theta_3}{dz'} &= i\kappa_3 E_1 E_2 \hat{\boldsymbol{\theta}}_{3,\perp} \cdot (\underline{\mathbf{d}}' : \hat{\boldsymbol{\theta}}_1 \hat{\boldsymbol{\theta}}_2) = i\kappa_3 E_1 E_2 f_{3,\perp}(\theta_3; \theta_1, \theta_2)\end{aligned}\quad (6)$$

where  $\underline{\mathbf{d}}' = \underline{\mathbf{d}}/2d_{36}$  and  $\kappa_i = 2\epsilon_0 d_{36} \gamma_i = \omega_i d_{36} / n_i c$ .

In Eq. (6), we define the functions

$$\begin{aligned}f_i(\theta_i; \theta_j, \theta_k) &= \hat{\boldsymbol{\theta}}_i \cdot (\underline{\mathbf{d}}' : \hat{\boldsymbol{\theta}}_j \hat{\boldsymbol{\theta}}_k) \\ f_{i,\perp}(\theta_i; \theta_j, \theta_k) &= \hat{\boldsymbol{\theta}}_{i,\perp} \cdot (\underline{\mathbf{d}}' : \hat{\boldsymbol{\theta}}_j \hat{\boldsymbol{\theta}}_k).\end{aligned}\quad (7)$$

The  $f_i$  functions represent the projections of the nonlinear susceptibility tensor onto the field polarization directions. The first three equations in Eq. (6) are the same in structure as the usual three-wave mixing equations, with the strength of the coupling modified by the  $f_i$  functions. As seen in Eq. (7), calculation of the  $f_i$  functions is the same calculation as involved in evaluating the effective nonlinear coefficient in the conventional three-wave case. An important difference is that in the six-wave case, the strength of the coupling can change as the polarization states of the interacting waves evolve. The second three equations in Eq. (6) describe the evolution of the angles  $\theta_i$ . If  $\theta_i$  varies with  $z'$ , then the  $f_i$  will also depend on  $z'$ . The evolution of each of the  $\theta_i$  is

driven by the orthogonal component of the nonlinear polarization,  $\hat{\theta}_{i,\perp} \cdot \mathbf{P}^{(2)}(\omega_i)$  or equivalently by  $f_{i,\perp}$ . When  $f_{i,\perp}$  is non-zero, the transverse component of the nonlinear polarization,  $\mathbf{P}_{i,\text{trans}}^{(2)}$ , is not parallel to  $\mathbf{E}_i$ , and so the polarization angle  $\theta_i$  will evolve with  $z'$ .

The polarization-angle evolution equations in Eq. (6) show that  $d\theta_i/dz'$  is proportional to  $1/E_i$ , which implies that when the field amplitude at  $\omega_i$  is small, the orientation angle of that field is more easily changed compared to when  $E_i$  is large. As a result, we would expect that when a wave has very little power (either at the initial portion of an interaction or when it becomes highly depleted), its orientation angle may change rapidly.

For a down-conversion process where the initial idler field is zero, but  $E_3(0)$  and  $E_2(0)$  are non-zero, the idler angle equation dictates that  $f_{i,\perp} = 0$  at  $z' = 0$  in order for  $d\theta_1/dz'$  to be finite (since  $d\theta_1/dz' \propto 1/E_1$ ). The condition  $f_{i,\perp} = 0$  is mathematically identical to the stipulation that  $\theta_1$  is chosen to maximize the gain (or magnitude of  $f_1$ ) for given  $\theta_2$  and  $\theta_3$ . Similar considerations apply for a sum-frequency or second-harmonic generation process where  $E_3(0)$  vanishes.

### 3. Manley-Rowe relations

Even though the polarization orientation angles of the waves may change, Manley-Rowe relations [23] still apply. The intensity at frequency  $\omega_i$  is given by  $I(\omega_i) = \epsilon_0 c n_i E_i^* E_i / 2$ , so the change in intensity with respect to  $z'$  is

$$\frac{dI(\omega_i)}{dz'} = \frac{\epsilon_0 c n_i}{2} \left( E_i^* \frac{dE_i}{dz'} + E_i \frac{dE_i^*}{dz'} \right). \quad (8)$$

If we multiply the three amplitude equations in Eq. (6) by  $E_1^*$ ,  $E_2^*$ , and  $E_3^*$ , respectively, add each equation's complex conjugate, and then compare terms, we see that if

$$f_1(\theta_1; \theta_2, \theta_3) = f_2(\theta_2; \theta_3, \theta_1) = f_3^*(\theta_3; \theta_1, \theta_2) \quad (9)$$

holds, then the Manley-Rowe relations

$$\frac{1}{\omega_1} \frac{dI(\omega_1)}{dz'} = \frac{1}{\omega_2} \frac{dI(\omega_2)}{dz'} = -\frac{1}{\omega_3} \frac{dI(\omega_3)}{dz'} \quad (10)$$

are obeyed.

In lossless media, the components of  $\underline{\mathbf{d}}$  are real quantities [24, 25], and also exhibit full permutation symmetry [24, 26]. We only consider linear polarization states and therefore, all  $f_i$  functions are real. These properties validate Eq. (9), and therefore the Manley-Rowe relations hold. The Manley-Rowe relations can be shown to be obeyed by circular and elliptical polarization states where the  $f_i$  functions are complex. The proof for complex polarization states and for a general propagation direction in zincblende crystal is given in the Appendix. It is worth noting that a naive calculation of nonlinear mixing for just one polarization component at each frequency, rather than both as done here, can yield different effective nonlinear coefficients for up-conversion compared to down-conversion, and hence an apparent violation of Manley-Rowe relations (see Appendix B and figure B.1 in [22]).

Eq. (9) simplifies the notation and allows us to write  $f_i(\theta_i; \theta_j, \theta_k) = f(\theta_i, \theta_j, \theta_k) = f$ . Once the function  $f$  is derived for a particular propagation geometry, then  $f_{i,\perp}$  can be calculated using

$$f_{i,\perp}(\theta_i; \theta_j, \theta_k) = \frac{\partial f}{\partial \theta_i}. \quad (11)$$

Calculation of the  $f$  function is effectively the same as calculating the polarization dependence of  $d_{\text{eff}}$  (as described in [11, 19, 22]). For example, the  $f$  and  $f_{i,\perp}$  functions for the case of  $\hat{\mathbf{k}} || [\bar{1}10]$ ,

$\hat{\mathbf{a}}||[110]$  and  $\hat{\mathbf{b}}||[001]$  in a zincblende crystal are

$$\begin{aligned}
 f &= \sin \theta_1 \cos \theta_2 \cos \theta_3 + \cos \theta_1 \sin \theta_2 \cos \theta_3 + \cos \theta_1 \cos \theta_2 \sin \theta_3 \\
 f_{1,\perp} &= \cos \theta_1 \cos \theta_2 \cos \theta_3 - \sin \theta_1 \sin \theta_2 \cos \theta_3 - \sin \theta_1 \cos \theta_2 \sin \theta_3 \\
 f_{2,\perp} &= -\sin \theta_1 \sin \theta_2 \cos \theta_3 + \cos \theta_1 \cos \theta_2 \cos \theta_3 - \cos \theta_1 \sin \theta_2 \sin \theta_3 \\
 f_{3,\perp} &= -\sin \theta_1 \cos \theta_2 \sin \theta_3 - \cos \theta_1 \sin \theta_2 \sin \theta_3 + \cos \theta_1 \cos \theta_2 \cos \theta_3.
 \end{aligned} \tag{12}$$

The permutation symmetry among  $\theta_1$ ,  $\theta_2$ , and  $\theta_3$  in  $f$  is apparent in the first equation.

For difference frequency generation where the initial angles  $\theta_2$  and  $\theta_3$  are fixed, the idler emerges at the angle where  $f$  is maximized. By setting  $\partial f / \partial \theta_1 = 0$  and solving for  $\theta_1$  in Eq. (12), we find that

$$\begin{aligned}
 \tan \theta_1 &= \frac{\cos \theta_2 \cos \theta_3}{\sin(\theta_2 + \theta_3)} \\
 f &= \sqrt{\sin^2(\theta_2 + \theta_3) + \cos^2 \theta_2 \cos^2 \theta_3} \\
 &= \sqrt{\cos^2 \theta_2 + \sin^2 \theta_2 \cos^2 \theta_3 + 2 \cos \theta_2 \cos \theta_3 \sin \theta_2 \sin \theta_3}.
 \end{aligned} \tag{13}$$

These agree with expressions for the effective nonlinear coefficient in [19, 22]. Eq. (13) can be applied to sum-frequency generation by interchanging the roles of  $\theta_1$  and  $\theta_3$ .

#### 4. Effective gain reduction in OPOs and OPAs

The simultaneous phasematching of multiple polarizations in zincblende materials can lead to an apparent reduction in gain and conversion efficiency in nonlinear frequency conversion. The cause of the apparent gain reduction is phasematched back-conversion to a field at the pump frequency but polarized in a direction orthogonal to the original pump. The back-conversion process to the orthogonally polarized pump is an unseeded, cascaded process. In the absence of this process, generation of signal and idler would proceed until the pump becomes depleted, at which point back-conversion of the pump with a  $180^\circ$  phase inversion begins. However, in non-birefringent materials, both pump polarizations are phasematched, and if  $f_{3,\perp} \neq 0$ , back-conversion of the field at  $\omega_3$  polarized orthogonally to the original pump will begin as soon as finite amplitudes of the signal and idler fields are present. This back-generated field together with the remaining pump field in the input polarization will manifest as a rotation of the polarization angle of the pump field.

We examine the effective gain reduction associated with polarization-independent phasematching in optical parametric amplification and show the close relationship between gain reduction and polarization rotation. We also look at a plane-wave OPO based on a quasi-phasematched zincblende crystal. The conversion efficiency and output polarization-orientation angles of the OPO differ from those quantities of an OPO with fixed polarization angles.

##### 4.1. Optical parametric amplification

In optical parametric amplification, a strong pump at frequency  $\omega_3$  amplifies a seed signal at  $\omega_2$  while producing an idler at  $\omega_1$  (with  $\omega_3 = \omega_1 + \omega_2$ ). Let us assume that the pump is undepleted

( $E_3 = E_{3,0}$ ) and that the idler is unseeded ( $E_1(0) = 0$ ). If  $\Delta k = 0$ , we find from Eq. (6)

$$\begin{aligned} \frac{d^2 E_1}{dz'^2} &= i\kappa_1 E_{3,0} \left( \frac{dE_2^*}{dz'} f + E_2^* \left( \frac{\partial f}{\partial \theta_1} \frac{d\theta_1}{dz'} + \frac{\partial f}{\partial \theta_2} \frac{d\theta_2}{dz'} + \frac{\partial f}{\partial \theta_3} \frac{d\theta_3}{dz'} \right) \right) \\ &= i\kappa_1 E_{3,0} \left( \frac{dE_2^*}{dz'} f + E_2^* \left( f_{1,\perp} \frac{d\theta_1}{dz'} + f_{2,\perp} \frac{d\theta_2}{dz'} + f_{3,\perp} \frac{d\theta_3}{dz'} \right) \right) \\ &= E_1 \left( \kappa_1 \kappa_2 |E_{3,0}|^2 |f|^2 - \kappa_1^2 \frac{(E_2^*)^2 E_{3,0}^2}{E_1^2} f_{1,\perp}^2 - \kappa_1 \kappa_2 E_{3,0}^2 \frac{E_1^* E_2^*}{E_1 E_2} f_{2,\perp}^2 - \kappa_1 \kappa_3 |E_2|^2 f_{3,\perp}^2 \right). \end{aligned} \quad (14)$$

In the previous section, we argued that if  $E_1(0) = 0$ , then  $f_{1,\perp} = 0$  at  $z' = 0$ . We can choose the polarization angle at  $\omega_2$  to maximize gain, which implies that  $\partial f / \partial \theta_2 = f_{2,\perp} = 0$  at  $z' = 0$ . In the low-conversion limit, we may approximate that  $f_{1,\perp} \approx 0$  and  $f_{2,\perp} \approx 0$  over the entire propagation length. With these simplifying assumptions, the last expression in Eq. (14) becomes

$$\frac{d^2 E_1}{dz'^2} = E_1 (\kappa_1 \kappa_2 |E_{3,0}|^2 |f|^2 - \kappa_1 \kappa_3 |E_2|^2 f_{3,\perp}^2). \quad (15)$$

Using similar arguments for the amplification of the signal at  $\omega_2$ , we find

$$\frac{d^2 E_2}{dz'^2} = E_2 (\kappa_1 \kappa_2 |E_{3,0}|^2 |f|^2 - \kappa_2 \kappa_3 |E_1|^2 f_{3,\perp}^2). \quad (16)$$

In Eqs. (15) and (16), we can identify  $\sqrt{\kappa_1 \kappa_2} |E_{3,0}| |f|$  as the OPA gain coefficient in the absence of polarization rotation. The second term on the right-hand sides of Eqs. (15) and (16) involving  $f_{3,\perp}$  are associated with back-conversion to the orthogonally polarized pump, which is manifested as rotation of the pump polarization from the initial orientation and reduction of the net OPA gain coefficient. Note that the gain reduction for  $E_1$  depends on the magnitude of the input signal compared to the pump. The reduction in gain for  $E_2$  depends on the magnitude of  $E_1$  compared to  $E_{3,0}$ ;  $|E_1|$  is small since we are assuming low-conversion and that the idler is initially unseeded, so the evolution of  $E_2$  will be dominated by the first term in Eq. (16). As the signal and idler grow with  $z'$ , the deviations in gain increase, ultimately violating the assumption of small pump depletion.

#### 4.2. Optical parametric oscillation

The gain and conversion efficiencies in optical parametric oscillators based on QPM zincblende materials will also be affected by phasematched back-conversion and evolution of the polarization angles. To frame the discussion, let us first recall a simple model of a phasematched ( $\Delta k = 0$ ), plane-wave, singly resonant OPO with low loss and low outcoupling, and single polarization states at the pump, signal and idler [27]. Eq. (6) suggests that the expressions in [27] can to first order be modified to include polarization-dependent gain by the substitution  $\kappa_i \rightarrow \kappa_i f$ . Thus, the gain in an OPO is related to the times above threshold,  $N$ , by

$$N = \left( \frac{E_3(0)}{E_{3,th}(0)} \right)^2 = \frac{\kappa_1 \kappa_2 f^2 E_3(0)^2 L^2}{a_s} = \frac{1}{\text{sinc}^2 \beta L}, \quad (17)$$

where  $E_3(0)$  is the pump amplitude at the crystal entrance,  $E_{3,th}(0)$  is the pump amplitude at oscillation threshold,  $L$  is the crystal length,  $a_s$  is the round-trip power loss at the signal, and

$$\beta = \sqrt{\kappa_1 \kappa_3} E_2 f. \quad (18)$$

This plane-wave OPO model assumes that variation in  $E_2$  with  $z'$  is small, which is appropriate for steady-state operation of a low-loss, low out-coupling OPO. The pump will be depleted

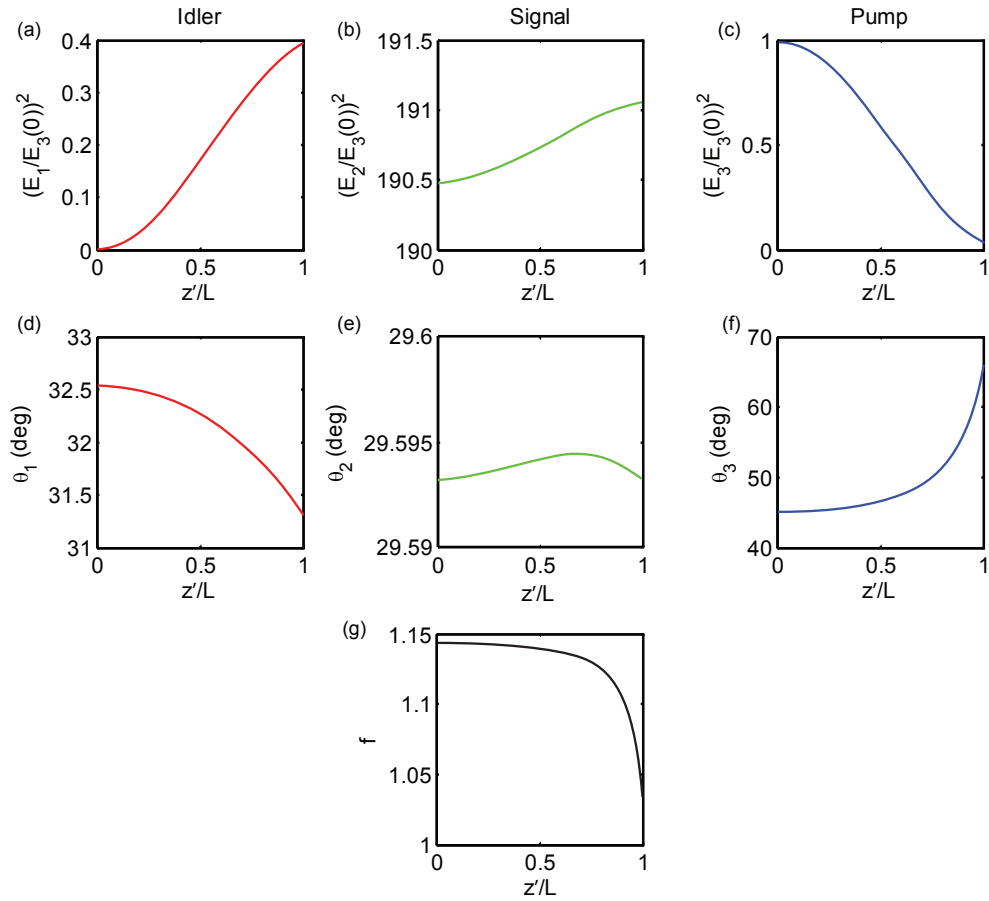


Fig. 1. Numerical modeling of a zincblende OPO including polarization rotation for the case of  $N = 2$ , 0.3% output coupling and pump polarization  $\theta_3(0) = 45^\circ$  to [110]. The top row (a)-(c) shows the relative intensities, the second row (d)-(f) shows the polarization angles, and the last row (g) shows the evolution of the function  $f$  as a function of crystal location.

according to

$$PD = \frac{I_3(0) - I_3(L)}{I_3(0)} = \sin^2 \beta L, \quad (19)$$

where PD represents pump depletion. If we assume all of the loss is from outcoupling ( $a_s = 1 - R$ ), then the external signal photon conversion efficiency,  $\eta'_2 = (1 - R)\omega_3 I_2(L)/(\omega_2 I_3(0))$ , is  $\eta'_2 = (\beta L)^2/N = PD$ . The problem with this model for non-birefringent media is that it does not account for the existence of polarization diversity in the six-wave interactions.  $f$  and  $\beta$  are not constant inside the OPO. The following numerical example illustrates the polarization rotation effects.

To examine these issues quantitatively, we compared the model that neglects polarization rotation effects to numerical modeling of a QPM zincblende OPO pumped at two times above threshold ( $N = 2$ ) and where all the losses are from outcoupling. For  $N = 2$ , an OPO will have conversion efficiency predicted by the above equations of  $\eta'_2 = 96.8\%$ . We performed the OPO simulation by integrating Eq. (6) over many roundtrips with appropriate boundary conditions and different initial pump polarization angles. We assumed 100% transmission of the pump and 100% reflection of the signal at the input coupler; 100% transmission of the pump and idler, and

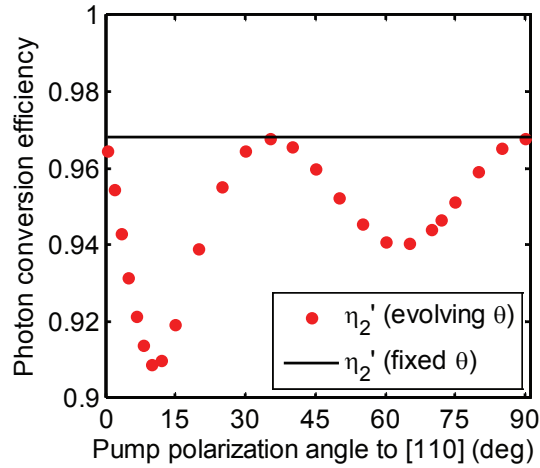


Fig. 2. Signal photon conversion efficiency,  $\eta_2'$ , as a function of pump angle for fixed times above threshold ( $N = 2$ ). As comparison, the solid line plots the prediction with the polarization angles fixed to maximize the gain at threshold.

$(1 - R) = 0.3\%$  transmission of the signal at the output coupler. We chose this low outcoupling for convenient comparison to the analytical low-loss results. The crystal was assumed to be lossless, and the sample geometry was  $\hat{\mathbf{k}} \parallel [\bar{1}10]$ ,  $\hat{\mathbf{a}} \parallel [110]$  and  $\hat{\mathbf{b}} \parallel [001]$ . In our calculations, we first calculated the optimal angles  $(\theta_{1,\text{opt}}, \theta_{2,\text{opt}})$  that maximized  $f$  for a given pump orientation  $\theta_3$  and hence the gain at threshold where cascading effects are absent. Eq. (18) allowed us to estimate  $E_2$  for given  $N$  and  $f(\theta_3, \theta_{1,\text{opt}}, \theta_{2,\text{opt}})$ . These optimal angles would be the polarizations expected from Eq. (12) if there were no polarization rotation effects. We used the optimal angles and the estimate for  $E_2$  as initial guesses for the OPO, then numerically propagated over many round trips until steady-state amplitudes and polarization angles were reached. Since  $E_1 = 0$  at the input of the crystal, we assumed the idler takes on the polarization orientation that optimizes  $f$  given the input pump polarization and the signal polarization found from the previous round trip.

Figure 1 shows results of the numerical modeling with the input pump polarized at  $45^\circ$  to  $[110]$ . The optimal signal and idler polarization angles that maximize  $f$  (and thus the effective nonlinearity) are  $\theta_{1,\text{opt}} = \theta_{2,\text{opt}} = 31.72^\circ$ . The plots show the steady-state intensities and polarization angles of the OPO as a function of position inside the nonlinear crystal as well as the evolution of the  $f$  function. The simulations in Fig. 1 show that the steady-state signal polarization angle was  $29.593^\circ$  and  $\eta_2' = 96.0\%$ . The polarization angle of the pump is significantly different at the exit of the crystal compared to the input ( $66.1^\circ$  vs.  $45^\circ$ ), which is an effect related to back-conversion to the orthogonally polarized pump.

To see the effects at different input pump polarization angles, we ran a family of simulations with fixed times above threshold. The  $f(\theta_3, \theta_{1,\text{opt}}, \theta_{2,\text{opt}})$  parameter varied with different input pump polarization angles, and hence from Eq. (17), we had to adjust the input pump intensity in order to hold  $N$  constant. Figure 2 plots external signal conversion efficiency for several different input pump polarizations with  $N = 2$  in the OPO simulations. We see in Fig. 2 that the conversion efficiencies are generally reduced. When the pump is polarized along  $[001]$  ( $90^\circ$ ) or along  $[111]$  ( $35.3^\circ$ ), the conversion efficiency match the fixed-angle cases; at these special orientations, the  $f_{i,\perp}$  functions go to zero and hence the polarization angles do not change. When the pump angle tends towards  $0^\circ$ , the conversion efficiencies for the simulations also approach the fixed-angle result,  $96.8\%$ .  $\theta_3 = 0^\circ$  corresponds to the interesting case of  $[110]$  pumping,

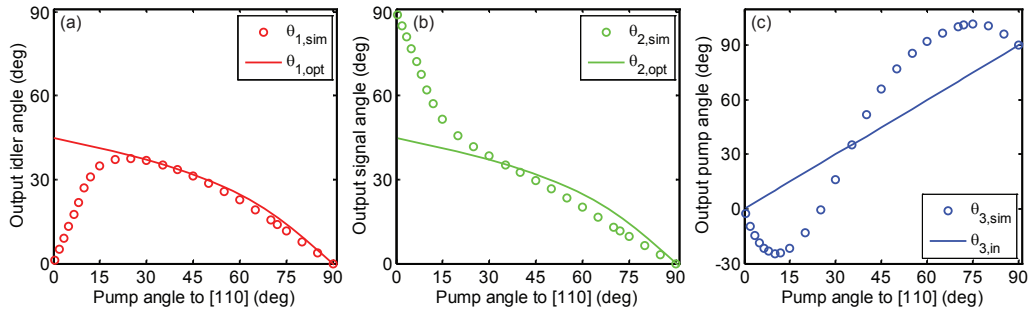


Fig. 3. Comparison of polarization angles at the output of the OPO if the polarization rotation effects are neglected ( $\theta_{i,\text{opt}}$ , solid line) or included ( $\theta_{i,\text{sim}}$ , open circles) for  $N = 2$ .

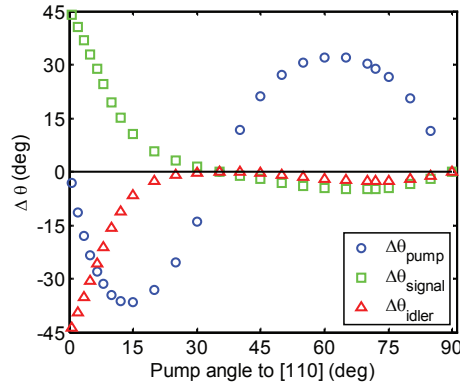


Fig. 4. Deviation of polarization angles ( $\theta_{i,\text{sim}} - \theta_{i,\text{opt}}$ ) for different initial pump angle in a zincblende OPO with times above threshold,  $N = 2$ .

which we discuss in greater detail later.

The output polarization-orientation angles in the OPO differ from optimal angles  $\theta_{i,\text{opt}}$  we expect from simply maximizing  $f$ . Fig. 3 shows the output polarization angles if the polarization rotation effects are included compared to  $\theta_{1,\text{opt}}$ ,  $\theta_{2,\text{opt}}$  and  $\theta_{3,\text{in}}$ . Figure 4 shows the deviations of the simulated output angles relative to the angles expected in the absence of polarization rotation. For the pump,  $\Delta\theta_3$  is the calculated output pump angle minus the input pump angle, and for the signal and idler,  $\Delta\theta_i = \theta_{i,\text{sim}} - \theta_{i,\text{opt}}$ . It should be noted that the  $\theta_{i,\text{opt}}$  are not necessarily the same as the polarization angles at  $z'/L = 0$  because the steady-state OPO incorporates angular changes of the signal and idler, even at  $z'/L = 0$  (examples of this effect are illustrated in Figs. 1(d) and 1(e)).

Comparing Figs. 2 and 4, we see a correlation between the decrease in OPO conversion efficiency and the magnitude of pump-angle change,  $|\Delta\theta_3|$ . When the pump is polarized along [001] or [111], the pump, signal and idler polarizations do not rotate away from the expected angles, and there is no decrease  $\eta'_2$  between the varying- and fixed-angle cases. As the pump approaches [110] polarization, the signal and idler angles deviate increasingly from  $\theta_{i,\text{opt}}$ . At  $\theta_3 = 0^\circ$ ,  $\theta_{1,\text{opt}} = \theta_{2,\text{opt}} = 45^\circ$ , but the OPO simulations instead show that  $\theta_1 \rightarrow 0^\circ$  and  $\theta_2 \rightarrow 90^\circ$ .

We also looked at simulation results at different times above threshold,  $N$ . These results as a function of  $N$  for three different incident pump polarization angles are presented in Fig. 5. Of the three cases, the conversion efficiencies were highest for  $\theta_3(0) = 90^\circ$  where the polarizations do not evolve, which was also seen in Fig. 2. Other pump polarization angles show reduced conversion efficiency, but as shown in Fig. 5(a), the reduction is modest. As  $N$  approaches  $(\pi/2)^2 = 2.47$  where full conversion is expected in a low-loss OPO [27], the pump becomes

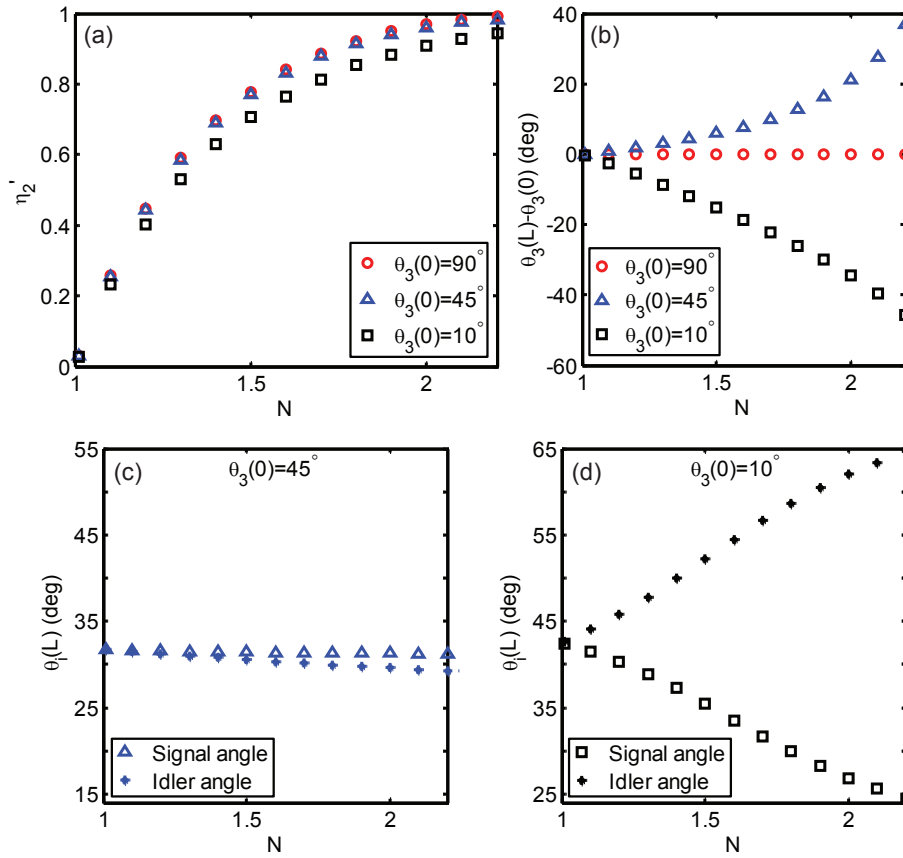


Fig. 5. Dependence on times above threshold,  $N$ , of (a) photon conversion efficiency and (b) deviation in pump polarization angle for several incident pump polarization angles.  $(1 - R)$  is set to 0.003. The signal and idler output polarization angles for (c)  $45^\circ$  and (d)  $10^\circ$  incident pump polarization angles.

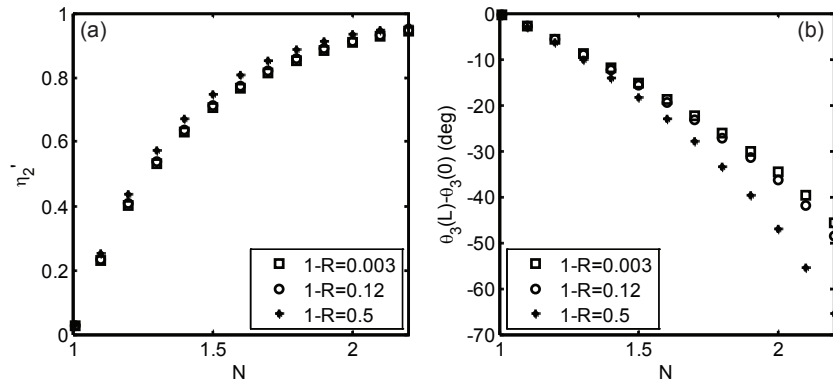


Fig. 6. Dependence on  $N$  of (a) photon conversion efficiency and (b) deviation in pump polarization angle for  $\theta_3(0) = 10^\circ$  and several different outcoupling rates.

strongly depleted and we observe large changes in the pump polarization angles (Fig. 5(b)). The signal and idler polarization angles also change more at large  $N$  (see in Figs. 5(c) and 5(d)). The magnitudes of the changes in  $\theta_1$  and  $\theta_2$  depend on  $\theta_3(0)$ .

We also examined the dependence of the zincblende OPO on outcoupling rate,  $(1 - R)$ , while still assuming  $a_s = 1 - R$ . Figure 6 plots the dependence of the photon conversion efficiency and the output pump polarization angle on  $N$  for  $1 - R = 0.003, 0.12, \text{ and } 0.5$ . The incident pump polarization angle was set to  $\theta_3(0) = 10^\circ$  in these simulations. There is a slight increase in  $\eta'_2$  with increasing outcoupling rate. Larger  $(1 - R)$  also produced larger deviations in pump polarization angles. Interestingly, changing  $(1 - R)$  did not affect the signal and idler polarization angles much, with simulation results for  $\theta_1$  and  $\theta_2$  almost identical to those shown in Fig. 5(d). We also looked at cases where OPO loss arose from both outcoupling and absorption loss at at the signal (that is,  $a_s > 1 - R$ ) and found the output intensities and polarization angles essentially depended only on the total round-trip loss and not on whether the loss was from absorption in the nonlinear medium or occurred at the output coupler.

## 5. Parametric processes with [110]-polarized pump

Pumping a parametric process in a QPM zincblende crystal with [110]-linearly-polarized light and  $\mathbf{k} \parallel [110]$  leads to interesting polarization effects. It has been noted in [10, 11, 16] that if the pump is exactly polarized along [110], then the gain becomes independent of the signal polarization, which is the basis for polarization-independent optical parametric amplification [16]. In this section, we examine [110]-polarized pumping in more detail.

Consider a down-conversion process where the pump is polarized along [110] ( $\theta_3 = 0^\circ$ ). Assuming that  $f_{i,\perp} = 0$  (which follows from choosing the idler polarization  $\theta_1$  to maximize gain), we can solve the second equation in Eq. (12) for  $\theta_1$  as a function of  $\theta_2$  and find that

$$\tan \theta_1 = \cot \theta_2. \quad (20)$$

Substituting this result for  $\theta_1$  back in expressions in Eq. (12) for  $f$ ,  $f_{2,\perp}$  and  $f_{3,\perp}$ , we find

$$\begin{aligned} |f| &= 1, \\ f_{2,\perp} &= 0, \\ f_{3,\perp} &= \frac{1}{2} \sin 2\theta_2. \end{aligned} \quad (21)$$

Together, Eqs. (20) and (21) show that in [110]-pumped down-conversion, the small-signal gain (proportional to  $f^2$ ) is independent of the signal polarization angle  $\theta_2$ . Eq. (20) implies that the idler will be polarized complementarily to the signal. Furthermore,  $f_{2,\perp} = 0$  automatically for this combination of signal and idler polarizations.

Equation (21) indicates that unless the signal polarization,  $\theta_2$ , is  $0^\circ, 90^\circ$ , etc.,  $f_{3,\perp}$  is non-zero and therefore the pump polarization will evolve away from [110] during propagation in the crystal. As  $\theta_3$  deviates from  $0^\circ$ , the function  $f$  and the gain are no longer independent of  $\theta_2$ .  $f$  will evolve with  $z'$  in cases of significant pump depletion, unless  $\theta_2 = 0^\circ, 90^\circ$ , etc. However, in optical parametric amplifiers where the pump power remains undepleted and much larger than either the signal or idler powers, the change of pump polarization will be small since  $|d\theta_3/dz'|$  is proportional to  $|E_1 E_2 / E_3|$ . Also, when  $\theta_3$  is near  $0^\circ$ ,  $f$  is only weakly dependent on  $\theta_2$ , so the gain in down-conversion can be nearly (but not quite) independent of  $\theta_2$ .

The gain in a [110]-pumped down-conversion process is identical when the signal polarization is along [110] or along [001]. With these polarization angles,  $f_{i,\perp} = 0$  for all waves (including the pump), so the angles will remain fixed during propagation in the crystal. Such a device is of interest for signal-processing functions such as dual-polarization wavelength conversion since two orthogonally polarized signal waves can be converted with the same efficiencies.

Identical conversion efficiencies for TE and TM polarizations were demonstrated using AlGaAs waveguides in [16]. However, signal waves polarized at angles other than  $\theta_2 = 0^\circ$  or  $90^\circ$  will experience slightly different gains as  $f_{3,\perp}$  and  $d\theta_3/dz'$  are no longer zero.

The analysis presented here suggests that a [110]-pumped OPO is equally likely to oscillate with  $(\theta_1, \theta_2)$  equal to  $(0^\circ, 90^\circ)$  or  $(90^\circ, 0^\circ)$ . At these angles,  $f_{i,\perp} = 0$  so the polarization-orientation angles do not evolve in the OPO, which explains why the simulated conversion efficiencies near  $\theta_3 = 0^\circ$  in Fig. 2 approach the fixed-angle  $\eta_2$  values. The OPO is less likely to oscillate with other angular combinations since the net gain is lower due to  $f_{3,\perp} \neq 0$ . The OPO essentially exhibits “polarization eigenstates” where it stably oscillates with equal efficiency at  $(\theta_1, \theta_2) = (0^\circ, 90^\circ)$  and  $(90^\circ, 0^\circ)$ . Since  $\theta_2 = 0^\circ$  and  $90^\circ$  mix equally well with the [110]-polarized pump, it should be possible to insert a half-wave plate inside an OPO cavity in a ring configuration (quarter-wave plate for a standing-wave OPO cavity) that rotates the polarization of the resonating signal wave by  $90^\circ$  on each round trip. The light will make two trips around the cavity to complete one round trip with amplification occurring on both trips through the crystal.

## 6. Applications and future work

The nonlinear optical processes described above are just a few examples of the interesting polarization dynamics arising from  $\chi^{(2)}$  mixing in QPM zincblende crystals. When all polarization states are phasematched to require six rather than three coupled-wave equations (described in Sections 2 and 3), the interactions of the additional three waves have similarities to simultaneously phasematched processes, such as cascaded sum-frequency generation [21] or other multistep parametric processes [28]. Most previous work on multistep processes has involved birefringent crystals such as PPLN or KTP. In these previous treatments of mixing of different polarization states, the discussions have typically involved multiple phase-mismatch factors or have ignored interactions of certain polarizations that are far away from phasematching. When mixing polarization states in a QPM zincblende crystal, the coupling coefficients for different polarization combinations can be similar in magnitude because of the highly symmetric nonlinear susceptibility tensor and the fact that there are no constraints from phasematching on which polarization states can interact. Hence it may be interesting to investigate nonlinear mixing in QPM zincblende semiconductors for the effects of all-optical signal processing through polarization switching [29–31].

## 7. Conclusion

Quasi-phasematching has allowed efficient nonlinear optical frequency conversion in bulk, isotropic media such as zincblende semiconductors. In these non-birefringent systems,  $\chi^{(2)}$  mixing is described by six rather than three coupled-wave equations since both polarization states at each of the three frequencies can participate in the interaction. The six coupled-wave equations can be cast in terms of amplitudes and polarization angles, which are similar in mathematical structure to the amplitude and phase equations in conventional three-wave mixing [23, 24]. Cascaded conversion into orthogonal polarization states can act like parasitic processes. We show that these cascaded processes can reduce conversion efficiencies in optical parametric oscillators and amplifiers based on QPM zincblende materials. Simultaneously phasematched processes in zincblende semiconductors lead to rich and complicated polarization dynamics with many opportunities for further exploration.

## Appendix. Manley-Rowe relations for general polarization states

The Manley-Rowe relations, dictating the exchange of energy in photon units, must be obeyed in cubic crystals as in any other case, though proper framing of the relation for isotropic media requires somewhat more care. If a single vector component of each field is considered at

each frequency, as is the case in conventional birefringent media, apparent violations of the Manley-Rowe relations can emerge; both transverse vector components of the field must be considered in evaluating the effective nonlinear coefficient, and the change in that coefficient as the polarization states evolve must be taken into account. Care must also be taken when using a complex basis, e.g. circular polarizations, for describing the polarization states of the fields.

To illustrate these points, we derive the Manley-Rowe relations in a form suitable for isotropic media, and with possibly complex polarization bases. We define the basis vectors orthogonal to propagation direction  $\hat{\mathbf{k}}$  as  $[\hat{\mathbf{a}}, \hat{\mathbf{b}}]$ , where

$$\begin{aligned}\hat{\mathbf{a}} &= \sum_i a_i \hat{\mathbf{i}} \\ \hat{\mathbf{b}} &= \sum_i b_i \hat{\mathbf{i}} \\ \hat{\mathbf{a}} \cdot \hat{\mathbf{a}}^* &= \hat{\mathbf{b}} \cdot \hat{\mathbf{b}}^* = 1 \\ \hat{\mathbf{a}} \cdot \hat{\mathbf{b}}^* &= 0.\end{aligned}\quad (22)$$

The unit vectors  $\hat{\mathbf{i}}$  represent the Cartesian directions  $(\hat{\mathbf{x}}, \hat{\mathbf{y}}, \hat{\mathbf{z}})$ , and the  $a_i$  and  $b_i$  coefficients may be complex. Examining Eqs. (10), (8) and (3), it is straightforward to show that the Manley-Rowe relations require that

$$(\mathbf{E}_3^* \cdot \mathbf{P}_3 + \mathbf{E}_3 \cdot \mathbf{P}_3^*) = (\mathbf{E}_2^* \cdot \mathbf{P}_2 + \mathbf{E}_2 \cdot \mathbf{P}_2^*) = (\mathbf{E}_1^* \cdot \mathbf{P}_1 + \mathbf{E}_1 \cdot \mathbf{P}_1^*). \quad (23)$$

Here, we use  $\mathbf{E}_i$  and  $\mathbf{P}_i$  to represent  $\mathbf{E}_i(z')$  and  $\mathbf{P}^{(2)}(z')$ , respectively. With the constitutive relations given by Eq. (2), Eq. (23) can be shown to require that

$$\mathbf{E}_3^* \cdot (\underline{\underline{\mathbf{d}}} : \hat{\mathbf{E}}_1 \hat{\mathbf{E}}_2) = \mathbf{E}_2 \cdot (\underline{\underline{\mathbf{d}}} : \hat{\mathbf{E}}_3 \hat{\mathbf{E}}_1^*) = \mathbf{E}_1 \cdot (\underline{\underline{\mathbf{d}}} : \hat{\mathbf{E}}_2^* \hat{\mathbf{E}}_3^*). \quad (24)$$

Expanding the fields for the first relation in Eq. (24) using the basis described in Eq. (22), we obtain

$$\begin{aligned}\sum_i \left[ (E_{3,a}^* a_i^* + E_{3,b}^* b_i^*) \sum_{j,k} d_{ijk}(-\omega_3; \omega_1, \omega_2) (E_{1,a} a_j + E_{1,b} b_j) (E_{2,a} a_k + E_{2,b} b_k) \right] = \\ \sum_k \left\{ (E_{2,a} a_k + E_{2,b} b_k) \left[ \sum_{i,j} d_{kij}(-\omega_2; \omega_3, -\omega_1) (E_{3,a} a_i + E_{3,b} b_i) (E_{1,a}^* a_j^* + E_{1,b}^* b_j^*) \right]^* \right\}.\end{aligned}\quad (25)$$

Recalling that  $\underline{\underline{\mathbf{d}}}(-\omega) = \underline{\underline{\mathbf{d}}}^*(\omega)$ , and in lossless media,  $\underline{\underline{\mathbf{d}}}$  is real and obeys overall permutation symmetry, it follows that  $d_{kij}^*(-\omega_2; \omega_3, -\omega_1) = d_{kij}(\omega_2; -\omega_3, \omega_1) = d_{ijk}(-\omega_3; \omega_1, \omega_2)$  and we see that the equality in Eq. (25) is satisfied. The other equalities required for Eq. (23) can be shown similarly to hold. It can also be seen how the equalities can fail if only a single component of each field were considered, and that care must be taken for consistent use of complex polarization bases.

## Funding

Air Force Office of Scientific Research (FA9550-09-1-0233).

## References

1. M. M. Fejer, G. A. Magel, D. H. Jundt, and R. L. Byer, "Quasi-phase-matched second harmonic generation: tuning and tolerances," *IEEE J. Quantum Electron.* **28**, 2631–2654 (1992).
2. C. B. Ebert, L. A. Eyres, M. M. Fejer, and J. S. Harris, "MBE growth of antiphase GaAs films using GaAs/Ge/GaAs heteroepitaxy," *J. Cryst. Growth* **201–202**, 187–193 (1999).

3. S. Koh, T. Kondo, Y. Shiraki, and R. Ito, "GaAs/Ge/GaAs sublattice reversal epitaxy and its application to nonlinear optical devices," *J. Cryst. Growth* **227–228**, 183–192 (2001).
4. L. A. Eyres, P. J. Tourreau, T. J. Pinguet, C. B. Ebert, J. S. Harris, M. M. Fejer, L. Becouarn, B. Gerard, and E. Lallier, "All-epitaxial fabrication of thick, orientation-patterned GaAs films for nonlinear optical frequency conversion," *Appl. Phys. Lett.* **79**, 904–906 (2001).
5. A. C. Lin, M. Fejer, and J. S. Harris, "Antiphase domain annihilation during growth of GaP on Si by molecular beam epitaxy," *J. Cryst. Growth* **363**, 258–263 (2013).
6. P. G. Schunemann, K. T. Zawilski, L. A. Pomeranz, D. J. Creeden, and P. A. Budni, "Advances in nonlinear optical crystals for mid-infrared coherent sources," *J. Opt. Soc. Am. B* **33**, D36–D43 (2016).
7. L. Becouarn, B. Gerard, M. Brevignon, J. Lehoux, Y. Gourdel, and E. Lallier, "Second harmonic generation of CO<sub>2</sub> laser using thick quasi-phase-matched GaAs layer grown by hydride vapour phase epitaxy," *Electron. Lett.* **34**, 2409–2410 (1998).
8. T. Skauli, K. L. Vodopyanov, T. J. Pinguet, A. Schober, O. Levi, L. A. Eyres, M. M. Fejer, J. S. Harris, B. Gerard, L. Becouarn, E. Lallier, and G. Arisholm, "Measurement of the nonlinear coefficient of orientation-patterned GaAs and demonstration of highly efficient second-harmonic generation," *Opt. Lett.* **27**, 628–630 (2002).
9. L. P. Gonzalez, D. C. Upchurch, P. G. Schunemann, L. Mohnkern, and S. Guha, "Second-harmonic generation of a tunable continuous-wave CO<sub>2</sub> laser in orientation-patterned GaAs," *Opt. Lett.* **38**, 320–322 (2013).
10. K. L. Vodopyanov, O. Levi, P. S. Kuo, T. J. Pinguet, J. S. Harris, M. M. Fejer, B. Gerard, L. Becouarn, and E. Lallier, "Optical parametric oscillation in quasi-phase-matched GaAs," *Opt. Lett.* **29**, 1912–1914 (2004).
11. P. S. Kuo, K. L. Vodopyanov, M. M. Fejer, X. Yu, J. S. Harris, D. F. Bliss, and D. Weyburne, "GaAs optical parametric oscillator with circularly polarized and depolarized pump," *Opt. Lett.* **32**, 2735–2737 (2007).
12. C. Kieleck, M. Eichhorn, A. Hirth, D. Faye, and E. Lallier, "High-efficiency 20–50 kHz mid-infrared orientation-patterned GaAs optical parametric oscillator pumped by a 2  $\mu$ m holmium laser," *Opt. Lett.* **34**, 262–264 (2009).
13. K. Devi, P. G. Schunemann, and M. Ebrahim-Zadeh, "Continuous-wave, multimilliwatt, mid-infrared source tunable across 6.4–7.5  $\mu$ m based on orientation-patterned GaAs," *Opt. Lett.* **39**, 6751–6754 (2014).
14. K. L. Vodopyanov, I. Makasyuk, and P. G. Schunemann, "Grating tunable 4 - 14  $\mu$ m GaAs optical parametric oscillator pumped at 3  $\mu$ m," *Opt. Express* **22**, 4131–4136 (2014).
15. P. G. Schunemann, L. A. Pomeranz, and D. J. Magarrell, "Optical parametric oscillation in quasi-phase-matched GaP," *Proc. SPIE* **9347**, 93470J (2015).
16. S. J. B. Yoo, C. Caneau, R. Bhat, M. A. Koza, A. Rajhel, and N. Antoniadis, "Wavelength conversion by difference frequency generation in AlGaAs waveguides with periodic domain inversion achieved by wafer bonding," *Appl. Phys. Lett.* **68**, 2609–2611 (1996).
17. O. Levi, T. J. Pinguet, T. Skauli, L. A. Eyres, K. R. Parameswaran, J. S. Harris, M. M. Fejer, T. J. Kulp, S. E. Bisson, B. Gerard, E. Lallier, and L. Becouarn, "Difference frequency generation of 8- $\mu$ m radiation in orientation-patterned GaAs," *Opt. Lett.* **27**, 2091–2093 (2002).
18. S. Vasilyev, S. Schiller, A. Nevsky, A. Grisard, D. Faye, E. Lallier, Z. Zhang, A. J. Boyland, J. K. Sahu, M. Ibsen, and W. A. Clarkson, "Broadly tunable single-frequency CW mid-infrared source with milliwatt-level output based on difference-frequency generation in orientation-patterned GaAs," *Opt. Lett.* **33**, 1413–1415 (2008).
19. S. Guha, J. O. Barnes, and P. G. Schunemann, "Mid-wave infrared generation by difference frequency mixing of continuous wave lasers in orientation-patterned gallium phosphide," *Opt. Mater. Express* **5**, 2911–2923 (2015).
20. G. Insero, C. Clivati, D. D'Ambrosio, P. D. Natale, G. Santambrogio, P. G. Schunemann, J.-J. Zondy, and S. Borri, "Difference frequency generation in the mid-infrared with orientation-patterned gallium phosphide crystals," *Opt. Lett.* **41**, 5114–5117 (2016).
21. P. S. Kuo, K. L. Vodopyanov, M. M. Fejer, D. M. Simanovskii, X. Yu, J. S. Harris, D. Bliss, and D. Weyburne, "Optical parametric generation of a mid-infrared continuum in orientation-patterned GaAs," *Opt. Lett.* **31**, 71–73 (2006).
22. P. S. Kuo, "Thick film, orientation-patterned gallium arsenide for nonlinear optical frequency conversion," Ph.D. thesis, Stanford University (2008).
23. Y. R. Shen, *The Principles of Nonlinear Optics* (Wiley-Interscience, New York, 1984).
24. J. A. Armstrong, N. Bloembergen, J. Ducuing, and P. S. Pershan, "Interactions between light waves in a nonlinear dielectric," *Phys. Rev.* **127**, 1918–1939 (1962).
25. N. Bloembergen, *Nonlinear Optics* (W. A. Benjamin, New York, 1965).
26. R. W. Boyd, *Nonlinear Optics* (Academic Press, San Diego, 2003), 2nd ed.
27. S. E. Harris, "Tunable optical parametric oscillators," *Proc. IEEE* **57**, 2096–2113 (1969).
28. S. M. Seltiel, A. A. Sukhorukov, and Y. S. Kivshar, "Multistep parametric processes in nonlinear optics," in *Progress in Optics*, vol. 47 E. Wolf, ed. (2005), pp. 1–73.
29. G. Assanto, S. Trillo, and I. Torelli, "All-optical processing by means of vectorial interactions in second-order cascading: novel approaches," *Opt. Lett.* **19**, 1720–1722 (1994).
30. S. Seltiel and Y. Deyanova, "Polarization switching as a result of cascading of two simultaneously phase-matched quadratic processes," *Opt. Lett.* **24**, 1296–1298 (1999).
31. M. A. Krumbügel, J. N. Sweetser, D. N. Fittinghoff, K. W. DeLong, and R. Trebino, "Ultrafast optical switching by use of fully phase-matched cascaded second-order nonlinearities in a polarization-gate geometry," *Opt. Lett.* **22**, 245–247 (1997).